





Article

Impacts of Human Activity and Global Changes on Future Morphodynamics within the Tien River, Vietnamese Mekong Delta

Christian Jordan ^{1,*}, Jan Visscher ¹, Nguyen Viet Dung ², Heiko Apel ² and Torsten Schlurmann ¹

¹ Ludwig-Franzius-Institute for Hydraulic, Estuarine and Coastal Engineering, Leibniz Universität Hannover, Nienburger Straße 4, 30167 Hannover, Germany; visscher@lufi.uni-hannover.de (J.V.); schlurmann@lufi.uni-hannover.de (T.S.)

² GFZ—German Research Center for Geoscience, Section Hydrology, Telegrafenberg, 14473 Potsdam, Germany; dung@gfz-potsdam.de (N.V.D.); hapel@gfz-potsdam.de (H.A.)

* Correspondence: jordan@lufi.uni-hannover.de

Received: 8 July 2020; Accepted: 31 July 2020; Published: 5 August 2020



Abstract: The hydro- and morphodynamic processes within the Vietnamese Mekong Delta are heavily impacted by human activity, which in turn affects the livelihood of millions of people. The main drivers that could impact future developments within the delta are local stressors like hydropower development and sand mining, but also global challenges like climate change and relative sea level rise. Within this study, a hydro-morphodynamic model was developed, which focused on a stretch of the Tien River and was nested into a well-calibrated model of the delta's hydrodynamics. Multiple scenarios were developed in order to assess the projected impacts of the different drivers on the river's morphodynamics. Simulations were carried out for a baseline scenario (2000–2010) and for a set of plausible scenarios for a future period (2050–2060). The results for the baseline scenario indicate that the Tien River is already subject to substantial erosion under present-day conditions. For the future period, hydropower development has the highest impact on the local erosion and deposition budget, thus amplifying erosional processes, followed by an increase in sand mining activity and climate change-related variations in discharge. The results also indicate that relative sea level rise only has a minimal impact on the local morphodynamics of this river stretch, while erosional tendencies are slowed by a complete prohibition of sand mining activity. In the future, an unfavourable combination of drivers could increase the local imbalance between erosion and deposition by up to 89%, while the bed level could be incised by an additional 146%.

Keywords: Mekong; numerical modelling; climate change; sea level rise; dam impacts; sand mining; river morphology

1. Introduction

The Vietnamese Mekong Delta (VMD), which is home to approximately 18 million people, is essential to the food security of Southeast Asia. Due to a mean delta elevation of 0.8 m [1], the low-lying delta is particularly vulnerable to direct human intervention such as hydropower dam operation [2,3] and sand mining [4–6] as well as global challenges like climate change-induced relative sea level rise (RSLR) [1,7,8].

Recently, the construction and operation of hydropower infrastructure within the Mekong River Basin (MRB) has led to a significant reduction of sediment supply to the delta region. At the beginning of this century, approximately 35 to 45 M t/yr of sediment, which represents approximately 25 to 32% of the total basin-wide sediment load, was trapped within the MRB caused by the operation of hydropower dams [9]. As of September 2017, 44 hydropower dams were under construction within the

MRB, with 212 additional dams having been commissioned [10]. Should all dams be built, the sediment supply to the South China Sea could be reduced by more than -95% [2,3]. In addition to a reduction in sediment supply, the construction and operation of hydropower dams within the MRB alter the monsoon-driven hydrological regime [11–14] and hinder fish migration [15].

Another important driver of changes in the local sediment supply and the morphological evolution of the Mekong River is unsustainable sand mining, which has recently gained attention within the scientific community [4–6,16,17]. Current estimates of sand extraction within the VMD are of the order of 7.7 to 28.0 M m³/yr [4–6,16], equivalent to 14.3 to 52.1 Mt/yr (assuming a dry density of 1.86 t/m³). Recent findings indicate that annual volumes of sand extraction could be even higher due to informal mining activity [6]. Impacts on hydrology, sediment transport, biodiversity and groundwater levels have been reported [18–20], indicating the manifold consequences of sand mining on the local environment. The sediment starvation within the VMD, resulting from the cumulative effects of hydropower infrastructure and sand mining, has also led to riverbank erosion [21,22], recessing coastlines [23–25] and the loss of coastal vegetation [26].

The local impacts of human activity are aggravated by global challenges like climate change and relative sea level rise (RSLR). Climate change is expected to alter the hydrology of the Mekong River, though the possible range of impacts on the river's flow regime is highly uncertain [27,28]. RSLR describes the cumulative effects of eustatic sea level rise, i.e., variations in the volume of the global oceans, and vertical motions of land with respect to the sea-surface. Local rates of eustatic sea level rise in the waters off the VMD are approximately 2 to 4 mm/yr [29], while average rates of land subsidence are of the order of 11 to 16 mm/yr [30,31]. Delta aggradation rates of around 0.3 to 1.8 mm/yr [32] are therefore too small to counter the effects of RSLR. Accordingly, the flood hazard is significant as up to 41% of the delta's area would be below the sea level in case of a RSLR of 0.5 m [1]. An increase in RSLR will also alter the flow regime and sediment dynamics within the VMD [3,11]. Furthermore, higher sea levels will move the salinity intrusion within the Mekong's channels further upstream [33].

The main objective of this study is to investigate the impacts of different drivers on future morphodynamic changes within the VMD, based on a set of reasonable scenarios of likely human activity and global changes. The effects of hydropower dam operation, sand mining, climate change and RSLR on the bed level evolution of the Mekong River are examined in detail. For this purpose, a high-resolution numerical model, which covers approximately 18 km of the Tien River branch, was set up. Nested into a large-scale delta model [3,32], the Tien River model gives insights into the relationships between the local sediment transport as well as hydro- and morphological processes. The model enables the quantifying of local morphological changes for possible future pathways of delta development, thus providing new and valuable information for strategic planning within the VMD.

2. Materials and Methods

2.1. Regional Setting

The Mekong River has a length of approximately 4900 km. Along its course from the source on the Tibetan Plateau to the river mouth at the South China Sea, the Mekong River crosses six countries (China, Myanmar, Thailand, Laos, Cambodia and Vietnam). The Western North Pacific and Indian monsoon lead to a pronounced wet season (June–October) within the MRB. Sediment transport and morphodynamic processes within the VMD are dominated by the amplified hydrodynamic forcing during the wet season [34,35]. Within the delta region, the Mekong River is divided into two main branches: the Tien River and Hau River.

This study focuses on a stretch of approximately 18 km of the Tien River branch, which was surveyed during the dry and wet season of 2018 [6] and provided valuable datasets for the set-up and validation of a high-resolution numerical model of the river's hydro- and morphodynamics. The study area is located between the city of Sa Dec and the bifurcation spot of the Tien River and the Co Chien River near Vinh Long (see Figure 1). Tides within the area exhibit a mixed, mainly

semi-diurnal character. Due to the interaction of tides and riverine discharge, currents within the study area are bidirectional, i.e., directed upstream during high tide and downstream during low tide. During the wet season, the monsoon-induced amplification in riverine discharge leads to currents being almost exclusively directed towards the ocean. Within the study area, water levels, discharges and suspended sediment concentrations (SSCs) are continuously measured at the hydrological station of My Thuan. Monthly mean discharges vary between approximately 1800 to 13,400 m³/s [35]. The annual sediment flux of about 21.3 Mt/yr [35] is dominated by cohesive sediments, with sand only contributing approximately 3.8 Mt/yr [36]. Bed load transport only marginally contributes to the total sediment flux (<1%) [6]. Bed aggregates within the study area mainly consist of fine to medium sands [6,37]. Mud content increases towards shallow areas with low flow velocities, while coarser bed aggregates are found at locations where deep scour holes have formed. The morphological activity within the investigated Tien River section is known to be high. Recent findings indicate that hydropower dam operation and sand mining have triggered bank erosion and the incision of the river's channel in recent years [6].

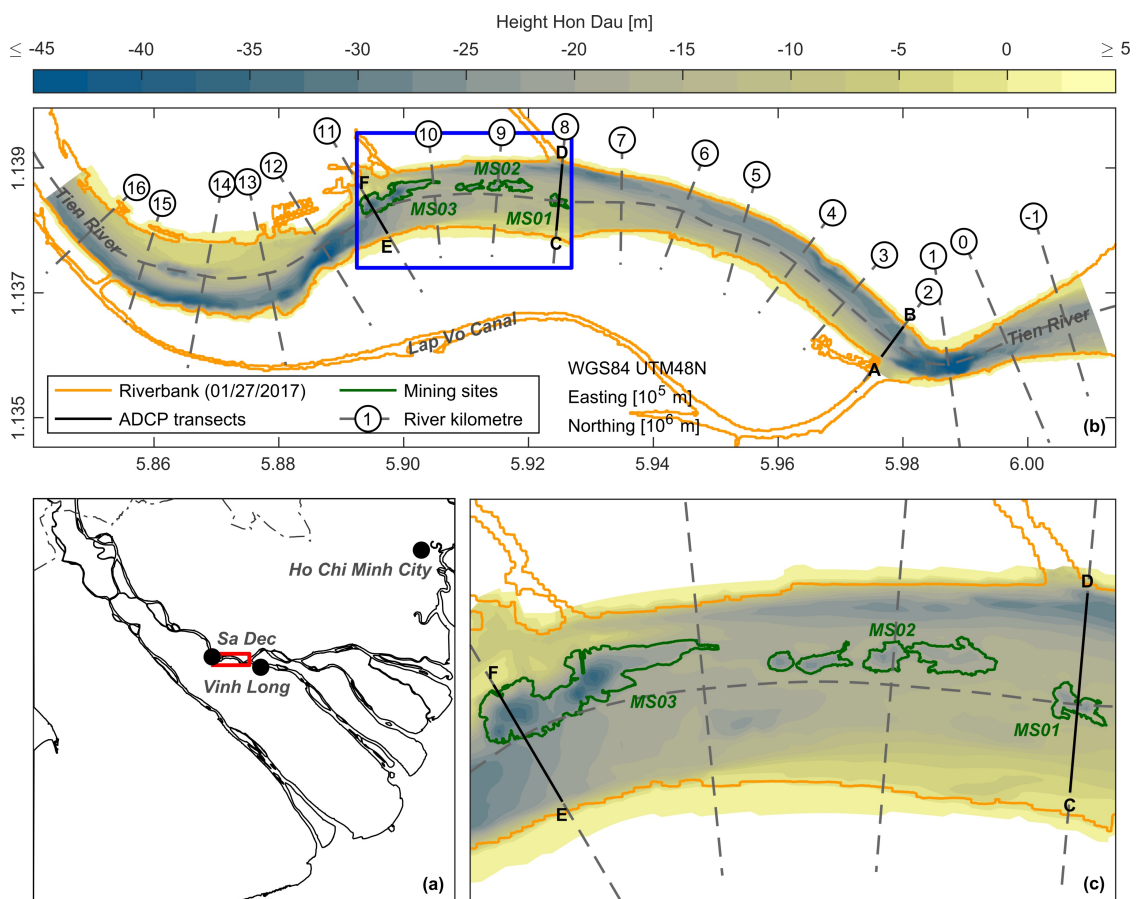


Figure 1. Location of the study area within the Vietnamese Mekong Delta (VMD). (a) Map of the VMD. Red box indicates the location of the study area, which is shown in more detail in panel (b). (b) Model domain, including bathymetry as well as positions of riverbanks, acoustic Doppler current profiler (ADCP) transects and sand mining sites MS01 to MS03. Riverbanks were extracted from historical Landsat-7 imagery using the modified normalised difference water index (MNDWI) [38]. Landsat-7 images courtesy of the United States Geological Survey (USGS), downloaded from the USGS EROS Centre (<https://earthexplorer.usgs.gov>). Sand mining sites were separated from the surrounding bathymetry using the approach in [6]. Blue box indicates river section between river kilometre marker (RKM) 8 to 11, which is shown in more detail in panel (c). (c) Detailed view of model domain between RKM 8 to 11.

2.2. Measured Data

To acquire datasets for the set-up and validation of a hydro-morphodynamic model of the study area, field surveys were conducted during the dry and wet seasons of 2018. Vessel-based surveys were carried out from 24 April to 19 May and 24 September to 10 October 2018, respectively. The bathymetry was surveyed via a multibeam echosounder (MBES) of type Reson SeaBat 7125 AUV, resulting in a high-resolution digital elevation model (DEM) of the river bed with a cell size of 1×1 m. Bathymetry data was later merged with an existing light detection and ranging (LiDAR) DEM of local topography data with a resolution of 5×5 m, which was provided by the Ministry of Natural Resources and Environment, Vietnam (MONRE). The local Hon Dau vertical datum was used as a height reference system. Water levels were measured via OTT Hydrolab HL4 multiparameter probes (CTDs) near the cities of Vinh Long and Sa Dec. Furthermore, an ADCP (Teledyne Workhorse Rio Grande 600 kHz) was used to monitor flow velocities and discharges along predefined transects. After the completion of the surveys, continuous measurements of water levels and discharges for the whole year of 2018, which were measured at the hydrological station of My Thuan, were provided by the Southern Regional Hydro-Meteorological Center, Vietnam (SRHMC). In order to also gain insight into the local bed aggregates, exemplary bed sediment samples were taken to derive grain-size distributions.

2.3. Model Set-Up

Using the software Delft3D [39], a numerical model of Tien River hydro-morphodynamics was set up to investigate the evolution of the local morphology. Based on a finite difference scheme, Delft3D solves the Reynolds-averaged Navier–Stokes equations on a staggered grid. A detailed description of the used formulations and implementation can be found in [39,40].

The domain of the numerical model has a horizontal grid resolution of approximately 25×50 m and covers a stretch of the Tien River of approximately 18 km. Bathymetry and topography data were interpolated onto the numerical grid. Closed model boundaries were implemented around 100 m landward from the current land–water interface, which was extracted from Landsat satellite images using the MNDWI [38]. Open boundaries were defined near the city of Sa Dec, downstream of the My Thuan bridge and at the confluence of the Mekong River with the Lap Vo Canal. Smaller distributaries within the model domain were neglected due to their low discharge. Due to the location of the open boundaries, the spatial extent of the model is slightly smaller than the study area described in [6]. Observed water levels and discharges were used to generate Riemann boundaries as hydrodynamic forcing along the open boundaries. For the model validation, observations from the 2018 dry and wet season were used as input, while hydrodynamic forcing was extracted from a quasi-2D hydrodynamic model of the whole VMD [3,32] for scenario simulations.

The majority of bed sediment samples revealed median grain diameters D_{50} in the range of 150 to 300 μm , in agreement with previous studies [37]. Larger particle sizes were only found in the vicinity of deep scour holes with maximum depths of up to 50 m, which have formed within the meandering riverbends. Thus, two representative sand fractions S1 (275 μm) and S2 (175 μm) were chosen for simulations. Sediment transport of sand fractions was modelled with the van Rijn TR2004 equation [41]. Due to the fine nature of suspended sediments within the Mekong River [42,43], an additional cohesive sediment fraction M1 (<63 μm) was used. The Partheniades–Krone formulations [44,45] were applied for the simulation of cohesive sediments. In order to make deposition a function of concentration and settling velocity [46], the critical shear stress for deposition τ_{crd} was set to 1000 N/m^2 . Being in agreement with the works in [47–49], the critical shear stress for erosion τ_{cre} was set to 0.2 N/m^2 . Based on previous numerical studies of the Mekong River, the settling velocity for fresh water $w_{s,f}$ was chosen to be 0.05 mm/s [47–50]. According to Stokes' Law, this settling velocity corresponds to a median grain diameter of approximately 7 μm . The settling velocity for saline water could be neglected, as salinity does not intrude into the study area. The constant erosion rate M was set to 2×10^{-5} $\text{kg}/(\text{m}^2 \text{s})$. For validation runs, equilibrium concentrations were used to reconstruct sediment input along the open boundaries. Measurements of sediment concentrations per fraction were unavailable for the full

duration of these runs. For scenario simulations, SSCs for all fractions were specified as boundary forcing. Therefore, SSCs for the mud fraction were directly extracted from a large-scale delta model for all scenarios [3,32]. For the baseline scenario, equilibrium concentrations of sand fractions were first stored along the boundaries. Based on these equilibrium concentrations, relative changes in the SSCs of the sand fractions for all scenarios were applied equivalent to relative changes in the mud fraction.

The bottom roughness within the river channel was specified by using spatially varying Manning (n) coefficients. Using the river's geometry and bed sediment samples as input, the application of the Brownlie bed roughness predictor [51] led to Manning coefficients in the range of 0.016 to 0.028 s/m^{1/3}. Based on previous findings [11], the bottom roughness for floodplains, i.e., areas above the mean water level, was set to 0.035 s/m^{1/3}.

2.4. Bed Layer Model

Due to the limited number of available samples of bed aggregates, a bed composition generation (BCG) run [52] was needed to generate a coherent initial bed sediment distribution for morphodynamic simulations. At the beginning of the BCG run, the three sediment fractions ($S1$, $S2$ and $M1$) were uniformly distributed across the whole model domain. To generate an initial bed sediment distribution in agreement with the start of the wet season, representative boundary conditions for the end of the dry season (April to May 2018) were used as model forcing. The simulation was run with a morphological acceleration factor f_{MORFAC} [53,54] of 100. Bed level updates were switched-off, thus only enabling a redistribution of the available sediment fractions for the fixed present-day bathymetry. When the sediment distribution in the bed remained nearly constant, a stable condition was reached. For this stable state, the amount of each fraction in the upper bed layer was extracted. The results of the BCG run are in good agreement with analysed bed sediment samples for the 2018 dry season (see Figure 2), showing the validity of the BCG approach for this study.

Ensuing morphodynamic runs with bed updating were carried out with a stratified bed layer model [52], i.e., an active transport layer on top of a limited number of buffering underlayers. The active layer is supplied with sediment from the underlayers in case of erosion, while sediment is stored in the underlayers in case of deposition. Correspondingly, the active layer, which defines the bed level, will rise or fall. Following the recommended approach of scaling the thickness of the active layer to the height of local bedforms [55], the transport layer thickness was chosen to be 0.75 m, being in agreement with dune heights within the study area. Additionally, 25 underlayers with a respective thickness of 1 m were implemented in the model, according to the local availability of deltaic sediments [17,56]. The sediment distribution for all layers was based on the results of the BCG run.

To prevent unrealistic channel incision, the transverse bed slope parameter (α_{bn}) was set to 50. To include the effect of bank erosion within the Delft3D model, the factor θ_{sd} was set to 0.5. Thus, dry cells along the land–water interface will be assigned 50% of the erosion of adjacent wet cells.

2.5. Model Validation

Simulations were initially run in three-dimensional configuration with 20 vertical sigma layers to validate the hydrodynamics within the model. The simulation results for this configuration were compared to measured ADCP profiles. Velocities were measured along transects A–B, C–D and E–F (see Figure 1) at different times during the 2018 dry season. Simulated and measured velocities were evaluated according to the relative error vector (REV) [57] to quantify the performance of the model. The REV is calculated as follows:

$$REV = \frac{\langle \sqrt{(u_{\text{meas}} - u_{\text{calc}})^2 + (v_{\text{meas}} - v_{\text{calc}})^2} \rangle}{\langle \sqrt{(u_{\text{meas}} + v_{\text{meas}})^2} \rangle} \quad (1)$$

where u_{calc} and v_{calc} are the simulated flow velocities in horizontal x- and y-direction, while u_{meas} and v_{meas} are the corresponding measured flow velocities. Angle brackets indicate the spatial averaging of mentioned parameters. A perfect model has a REV of 0. Table 1 provides a classification of model

performance with a $REV > 0$. According to the obtained REV values in the range between 0.19 to 0.37, the simulated flow velocities during low tide show good agreement compared to measurements (Figure 3). Similar model quality is also observed during high tide, with REV values of the order of 0.15 to 0.33 (Figure 4). Thus, the overall model performance for hydrodynamic simulations is considered good.

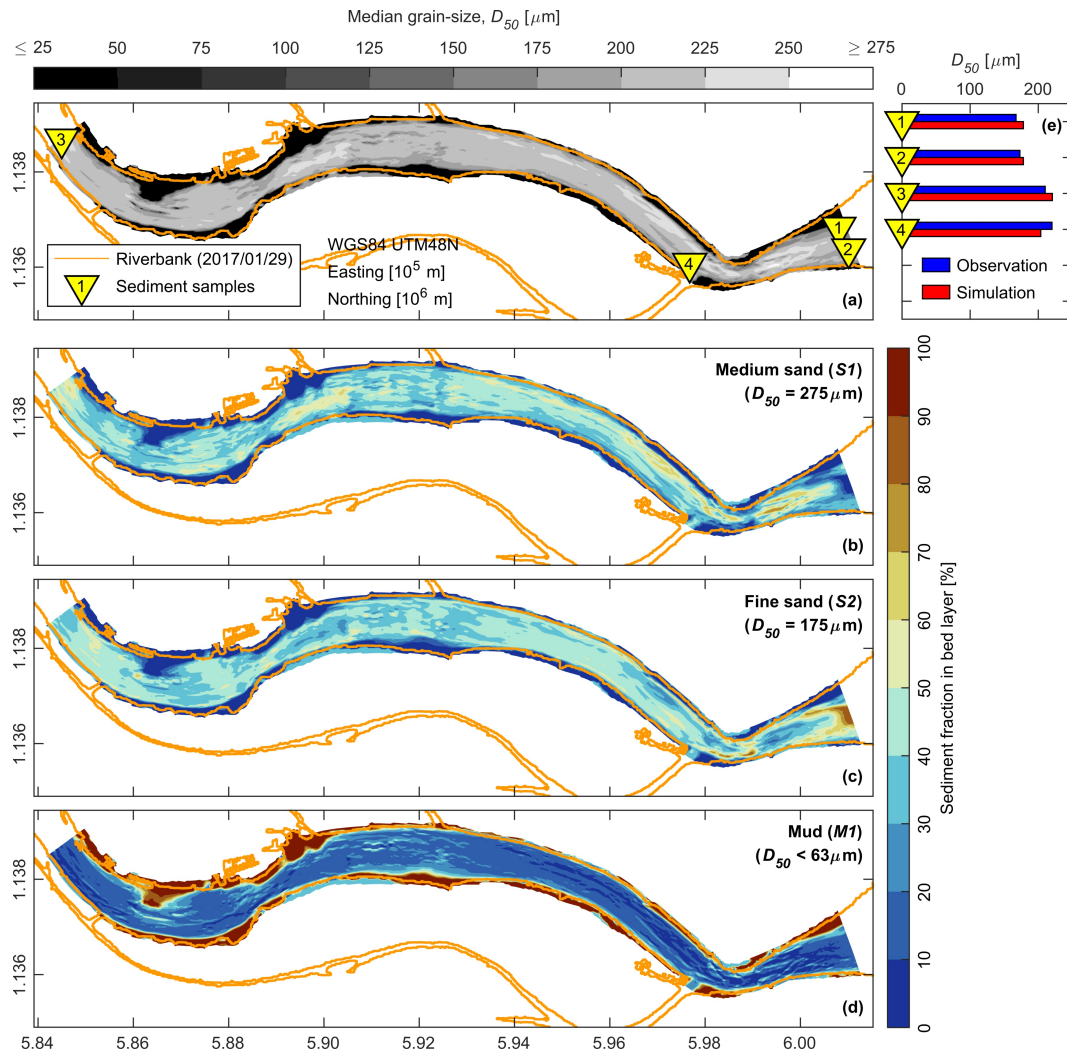


Figure 2. Bed sediment distribution at the end of the bed composition generation (BCG) run, including positions of riverbanks and selected bed sediment samples. Riverbanks were extracted from historical Landsat-7 imagery using the MNDWI [38]. Landsat-7 images courtesy of the USGS, downloaded from the USGS EROS Centre (<https://earthexplorer.usgs.gov>). (a) Median grain-size within the upper bed layer at the end of the BCG run. (b) Amount of sediment fraction S1 (medium sand) in the upper bed layer at the end of the BCG run. (c) Amount of fraction S2 (fine sand) in the upper bed layer at the end of the BCG run. (d) Amount of fraction M1 (mud) in the upper bed layer at the end of the BCG run. (e) Comparison of median grain-sizes between the numerical model and selected bed sediment samples. Locations of the samples are shown in panel (a).

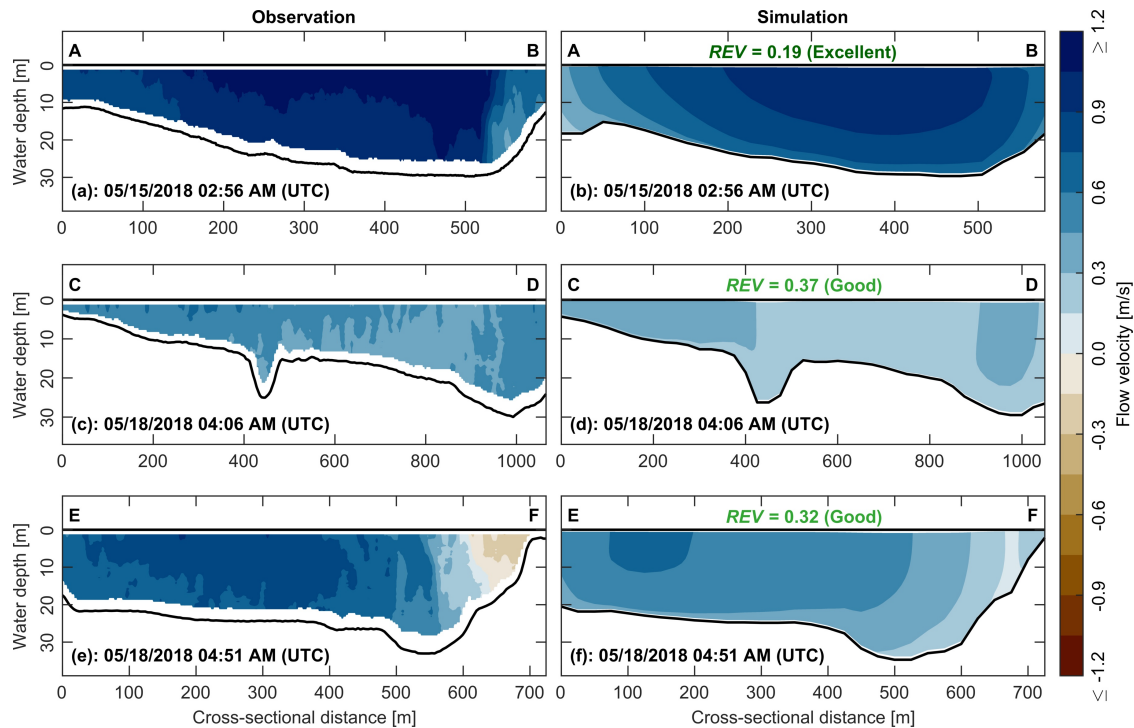


Figure 3. Comparison of measured and simulated currents along ADCP transects A–B, C–D and E–F during low tide for selected times of the 2018 dry season. (a) Measured flow velocities along transect A–B for 15 May 2018, 02:56 AM (UTC). (b) Simulated flow velocities along transect A–B and corresponding *REV* value for 15 May 2018, 02:56 AM (UTC). (c) Measured flow velocities along transect C–D for 18 May 2018, 04:06 AM (UTC). (d) Simulated flow velocities along transect C–D and corresponding *REV* value for 18 May 2018, 04:06 AM (UTC). (e) Measured flow velocities along transect E–F for 18 May 2018, 04:51 AM (UTC). (f) Simulated flow velocities along transect E–F and corresponding *REV* value for 18 May 2018, 04:51 AM (UTC). Negative velocities indicate flows in upstream direction, while positive velocities indicate flows in downstream direction.

As two- and three-dimensional simulations showed negligible differences in morphological changes, the model was run in depth-averaged mode for morphodynamic simulations. To assess the model performance for morphodynamic simulations, the adjusted Brier skill score (*BSSp*) [58] was used. The *BSSp* assesses anomalies in the model prediction and in measurements as follows:

$$BSSp = \frac{\langle (B - X)^2 \rangle - \langle (Y - X)^2 \rangle}{\langle (B - X)^2 \rangle - 2\langle \delta^2 \rangle} \quad (2)$$

where *B* is the initial bathymetry at the start of a simulation, *Y* is the predicted bathymetry at the end of a simulation, *X* is the corresponding measured bathymetry at the same time and δ is the measurement error. Due to the accuracy of the performed MBES measurements, a measurement error of 0.10 m was used for the calculation of the *BSSp*. The classification for the *BSSp* is shown in Table 1. In order to quantify the model quality for morphodynamic processes, the evolution of the sand mining sites *MS01* to *MS03* (see Figure 1) was simulated from 10 May to 10 October 2018. In contrast to other sand mining sites within the study area, these locations were surveyed in detail during both the 2018 dry and wet season, thus enabling the comparison of their observed morphological evolution to model results. According to *BSSp* values of 0.62 and 0.44 (see Figure 5c,f), the model performance can be considered good for reproducing the refilling process at mining sites *MS01* and *MS02*. Based on a *BSSp* of 0.06 (see Figure 5i), the model shows poor performance simulating the morphological evolution of mining site *MS03*. However, the model performance for this location is likely affected by neglecting dredging activity during the model validation, as information about the operation of dredgers between May to October 2018 was lacking. The measured validation data indicates that continuous dredging activity

was disturbing the refilling process at mining site MS03, leading to discrepancies between model results and observations. Accordingly, the overall model performance for morphodynamic processes is also considered good.

Table 1. Error classification for relative error vector (*REV*) and adjusted Brier skill score (*BSS_p*) according to the works in [57,58].

Classification	<i>REV</i>	<i>BSS_p</i>
Excellent	<0.20	0.80–1.00
Good	0.20–0.40	0.30–0.80
Reasonable	0.40–0.70	0.15–0.30
Poor	0.70–1.00	0.00–0.15
Bad	>1.00	<0.00

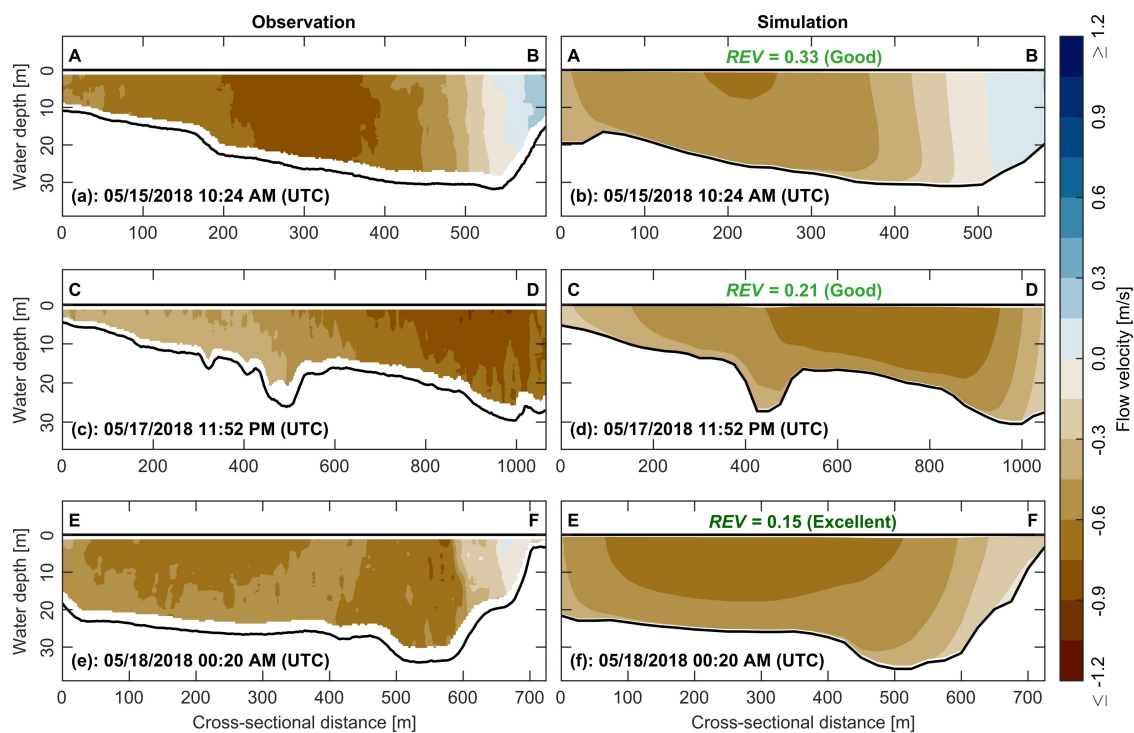


Figure 4. Comparison of measured and simulated currents along ADCP transects A–B, C–D and E–F during high tide for selected times of the 2018 dry season. (a) Measured flow velocities along transect A–B for 15 May 2018, 10:24 AM (UTC). (b) Simulated flow velocities along transect A–B and corresponding *REV* value for 15 May 2018, 10:24 AM (UTC). (c) Measured flow velocities along transect C–D for 17 May 2018, 11:52 PM (UTC). (d) Simulated flow velocities along transect C–D and corresponding *REV* value for 17 May 2018, 11:52 PM (UTC). (e) Measured flow velocities along transect E–F for 18 May 2018, 00:20 AM (UTC). (f) Simulated flow velocities along transect E–F and corresponding *REV* value for 18 May 2018, 00:20 AM (UTC). Negative velocities indicate flows in upstream direction, while positive velocities indicate flows in downstream direction.

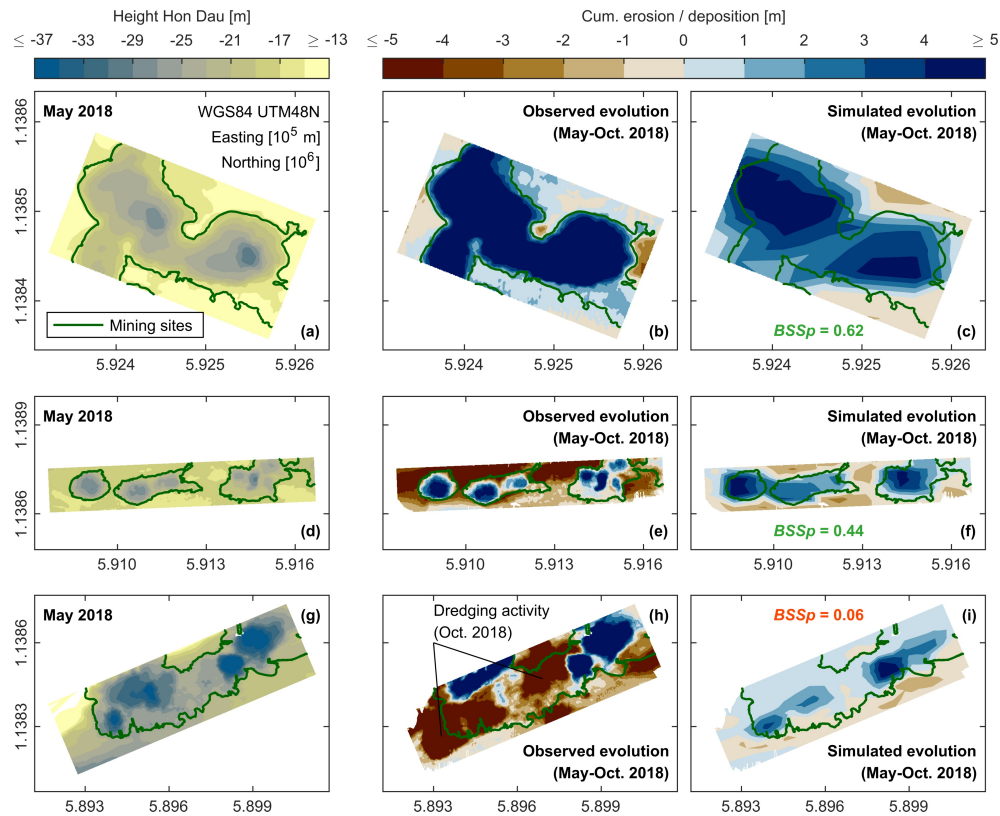


Figure 5. Comparison of measured and simulated morphological evolution at mining sites MS01 to MS03 from May to October 2018, including exact positions of these sand mining sites. Sand mining sites were separated from the surrounding bathymetry using the approach in [6]. (a) Measured bathymetry at mining site MS01 in early May 2018. (b) Observed morphological evolution at mining site MS01 from May to October 2018. (c) Simulated morphological evolution at mining site MS01 from May to October 2018 and corresponding $BSSp$ value. (d) Measured bathymetry at mining site MS02 in early May 2018. (e) Observed morphological evolution at mining site MS02 from May to October 2018. (f) Simulated morphological evolution at mining site MS02 from May to October 2018 and corresponding $BSSp$ value. (g) Measured bathymetry at mining site MS03 in early May 2018. (h) Observed morphological evolution at mining site MS03 from May to October 2018. (i) Simulated morphological evolution at mining site MS03 from May to October 2018 and corresponding $BSSp$ value.

2.6. Scenario Development

To assess the impact of plausible developments within the VMD on the morphodynamic processes within the Tien River, a baseline scenario and 23 future scenarios for local human activity and challenges on the global scale have been defined. The future scenarios are based on the combination of four different drivers and include variations in sediment supply and discharge caused by hydropower infrastructure (D), sand mining activity (M), variations in discharge associated with climate change (Q) and RSLR (S). It must be noted that two separate drivers were chosen to investigate the overall impact of climate change. Driver Q describes the climate change impact in the MRB and the associated effects on discharge and sediment flux at Kratie (Cambodia). Driver S describes the impact of climate change-related RSLR, which affects the lower boundary of the delta at the South China Sea. For all scenarios, hydrodynamic boundary conditions and time-series of SSCs were extracted along the open boundaries of the Delft3D model from a well-established quasi-2D hydrodynamic model of the whole delta [3,32]. The baseline period (2000–2010) was used as a reference, while the period 2050–2060 was used for the future scenarios. Applying the hydrograph shape with the highest probability within the VMD (see in [3] for details), simulations concentrated on the wet season between 16 July to 10 December. Additionally, different dredging strategies were directly applied to the bed level of the validated Tien River model.

For the future period, only the upper bound of a plausible range of changes was investigated for drivers D , Q and S , while a lower and upper bound were defined for sand mining. The upper bounds for D , Q and S were chosen in accordance with the work in [3]. The choice of upper bounds highlights maximum possible changes and ensures that the dominant drivers for the future morphological evolution of the study area can clearly be identified. Furthermore, the effects of the interaction of multiple drivers are amplified. The additional lower bound for sand mining highlights a possible future pathway that could help to mitigate the impacts of other drivers.

To analyse the impacts of hydropower development, both the discharge and sediment load were adapted for the upstream boundary of the delta model, which is located at Kratie. An upper bound for plausible changes in sediment load was defined by rescaling the maximum trapping efficiency of hydropower dams from [2] to the baseline period, resulting in a reduction of SSCs by approximately -95% . The upper bound of changes in the hydrograph was directly taken from [27], based on the assumption of 136 hydropower dams being operational within the MRB.

In order to investigate the impact of sand mining, different volumes of sand extraction were used for the baseline and future scenarios. For the baseline scenario, the recently observed volume of annual local sand mining activity by [6] was directly transferred to the domain of the Tien River model. Due to the slightly smaller study area, this resulted in a total extraction volume of $3.59 \text{ M m}^3/\text{yr}$. In accordance with the work in [6], this volume was distributed proportionally across all sand mining sites, which were identified during the 2018 dry and wet season (see Figure 6). Estimates of recent sand mining activity within the VMD indicate that extracted volumes have tripled or even quadrupled in recent decades [6,16]. As the impact of sand mining has gained more attention lately, even leading to the complete prohibition in some provinces, a similar increase of this magnitude seems unrealistic for the future period. Thus, a sand mining volume of $7.18 \text{ M m}^3/\text{yr}$ was defined as the upper bound, representing a doubling of present-day extraction rates (scenario M_+). A complete prohibition of sand mining activity was used as lower bound (scenario M_-).

To estimate the impact of climate change within the MRB, the hydrograph at the upstream boundary of the delta model was modified. For this driver, the upper bound by the authors of [27] was used. Within that study, average surface temperatures and monthly total precipitations from five general circulation models (GCMs) were used as input for a hydrological model of the MRB, while considering two different emission scenarios (IPCC SRES A1b and B1). Changes in discharge were mainly driven by the precipitations projected by the different GCMs.

In order to assess the impact of RSLR, the water level was increased by 0.63 m along the downstream boundary of the delta model, representing the upper end of local RSLR projections for the period 2046–2065. This upper limit combines the effects of deltaic aggradation and subsidence as well as eustatic sea level rise. Table 2 shows the notations, which are used for the different drivers. Additionally, the relative changes in discharge and SSCs at the open boundaries of the Tien River model as well as variations in the extraction volume, which are associated with the different drivers, are also summarised. The notation of the scenarios is a combination of the individual driver notation listed in Table 2.

Table 2. Notations used for single drivers and associated relative changes in discharges (Q_{BC}), sediment concentrations (SSC_{sBC}) and sand extraction volumes (V_{Extr}). Discharges and sediment concentrations were calculated along the model's boundaries by averaging hourly values over the duration of the simulation period. Percentages indicate changes in relation to the baseline scenario.

Drivers	Notation	Q_{BC}	SSC_{sBC}	V_{Extr}
Baseline	-	$12,577 \text{ m}^3/\text{s}$	$148.5 \text{ g}/\text{m}^3$	$3.59 \text{ M m}^3/\text{yr}$
Hydropower dams	D	-8%	-95%	0%
Increase in sand mining	M_+	0%	0%	$+100\%$
Decrease in sand mining	M_-	0%	0%	-100%
Climate change	Q	$+22\%$	$+12\%$	0%
RSLR	S	-5%	-2%	0%

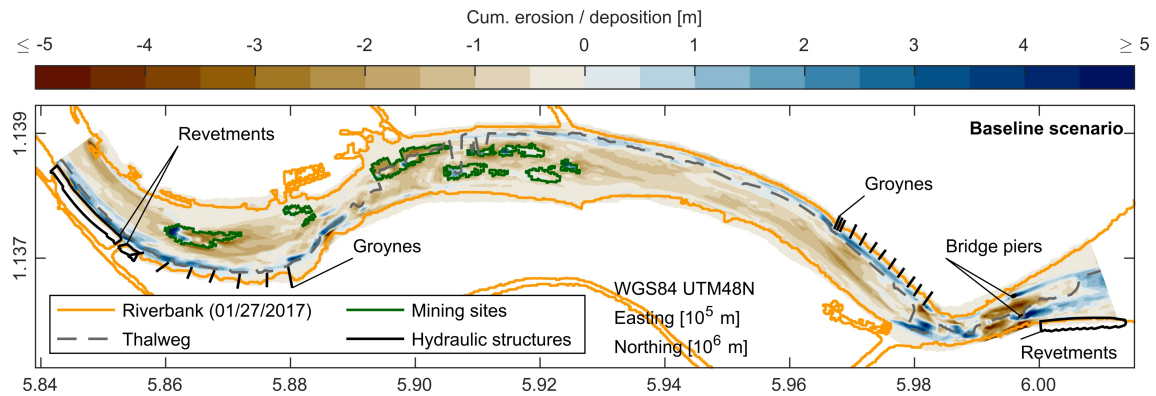


Figure 6. Pattern of cumulative erosion (red) and deposition (blue) at the end of the baseline scenario, including positions of riverbanks, the river’s thalweg, implemented sand mining sites and hydraulic structures. Riverbanks were extracted from historical Landsat-7 imagery using the MNDWI [38]. Landsat-7 images courtesy of the USGS, downloaded from the USGS EROS Centre (<https://earthexplorer.usgs.gov>). Sand mining sites were separated from the surrounding bathymetry using the approach in [6].

3. Results

In order to quantify the impacts of different drivers shown in Table 2 on the morphology of the study area, the resulting erosion and deposition patterns, tendencies of bed level incision and balances between erosion and deposition volumes were analysed in relation to the baseline scenario. Erosion and deposition patterns can be directly used to illustrate the formation and migration of riverine channels, test the effectiveness of hydraulic structures or to identify erosion-prone areas (e.g., riverbank erosion). In order to show how different scenarios amplify channel deepening, relative bed level changes were averaged across each cross section of the numerical model and subsequently projected onto a virtual RKM system (see Figure 1). Bed level changes, which are associated with the implementation of sand mining sites, were included in this calculation. To quantify the balance between erosion and deposition for all scenarios, the domain-wide volumes for erosion and deposition were calculated at the end of a simulation. Sand mining volumes were included in this calculation. For each scenario, the balance between erosion and deposition is given by the ratio of erosion volume to deposition volume ($R_{ero/dep}$). To gain better understanding of the results, the baseline scenario is presented first, followed by the impacts of single drivers and the cumulative impacts of multiple drivers.

3.1. Baseline Scenario

At the end of the baseline scenario, approximately 49% of the study area is subject to erosion, while 41% of the domain represents deposition (Figure 6). Areas with absolute bed level changes of less than ± 0.05 m were deemed insignificant and thus excluded from this calculation. At the end of the baseline period, the mean bed level changes are of the order of -0.13 m, illustrating a gradual incision of the river’s channel. This is in agreement with the domain-wide erosion volume (7.20 M m^3) exceeding the deposition volume (4.60 M m^3) by a factor of 1.57, indicating that the focus area can generally be characterised as an erosional environment. Deposition occurs near the river’s thalweg, with sediment being transported from shallower to deeper parts of the channel. In addition, the pattern displays the deposition of sediments in the vicinity of submerged groynes, which were installed in recent years to prevent continuous erosion of riverbanks [6]. High morphological activity can also be observed near the location of the My Thuan Bridge, where scouring processes have formed a deep pool. Furthermore, it becomes apparent that the refilling process at sand mining sites is hindered by continuous dredging activity, which was implemented for the baseline scenario.

3.2. Impact of Hydropower Development (Scenario D)

Figures 7 and 8 show how single drivers impact the erosion and deposition patterns in relation to the baseline scenario. Compared to the baseline, additional cumulative erosion represents areas experiencing more erosion as well as areas with less deposition. Equivalently, additional cumulative deposition combines areas that show less erosion or more deposition in relation to the baseline scenario. Hydropower development and the associated reduction of sediment supply and flood discharge lead to additional erosion within 58% of the study area, against only 9% of additional deposition and around 33% of insignificant bed level changes (Figure 7a). Additional erosion is prominent near the riverbanks, likely caused by a lack in the supply of fine sediments that normally would be deposited there. The tendency of bed level incision is amplified almost everywhere within the focus area for this scenario. In relation to the baseline scenario, the mean relative bed level changes are of the order of -0.08 m, equivalent to bed level incision increasing by approximately 62% (Figure 9). Moreover, the imbalance between erosion and deposition volumes within the study area also increases by around 43% ($R_{\text{ero/dep,D}} = 2.25$), caused by changes in the erosion and deposition volumes by 5% and -27% , respectively (Figure 10). It becomes apparent that these changes are non-proportional to a reduction of sediment supply by -95% , which was implemented as input along the open boundaries for this scenario. This illustrates how the morphological evolution of the river is only partly governed by the upstream and downstream supply of sediment. Local conditions like the availability of sediments along the riverbed, their mobilisation and redistribution also play a significant role in the morphological processes within the domain. Furthermore, the hydropower development also decreases the flood discharge during the wet season (see Table 2). The altered hydrodynamics reduce the flow velocities and bed shear stresses, leading to less pronounced bed level changes.

3.3. Impact of Sand Mining (Scenarios M_+ and M_-)

Compared to the baseline scenario, a doubling of the local sand extraction volume leads to additional erosion within 9% of the study area, while only 1% of the river experiences additional deposition (Figure 8a). As expected, the variability in bed level changes is highest between RKM7 to 15, corresponding to locations where sand mining activity was implemented. On average, the bed level incision exceeds the baseline scenario by -0.07 m, which is equivalent to an increase in channel deepening by approximately 54% (Figure 9). For this scenario, the total erosion volume increases by 16%, while the deposition volume is reduced by -6% , thus amplifying the prevailing imbalance in the local sediment budget ($R_{\text{ero/dep,M}_+} = 1.93$) (Figure 10). Inverse to an increase in sand mining activity, with a complete prohibition of local sand mining activity, 1% of the study area exhibits additional erosion, against 9% of additional deposition (Figure 8b). This scenario clearly has a positive effect on the local morphology, as illustrated by a mean rise of the bed level by around 0.07 m, therefore decreasing channel incision by approximately -54% (Figure 9). Simultaneously, the ratio of erosion and deposition volumes reduces to a value of 1.23, accompanied by a decrease in erosion volume by -11% and an increase in deposition volume by 13% (Figure 10). However, bed level changes are insignificant within most of the domain ($\sim 90\%$) for this upper and lower bound of future sand extraction. Changes in the erosion and deposition patterns are negligible a couple of kilometres upstream and downstream from locations of sand mining activity. For both scenarios, the sum of relative changes in the erosion and deposition volumes is of the same order as the respective changes in the amount of sand mining. This implies that sand mining does not necessarily cause regional losses of sediment beyond extracted volumes, but triggers a redistribution of local sediments in the vicinity of sand mining locations.

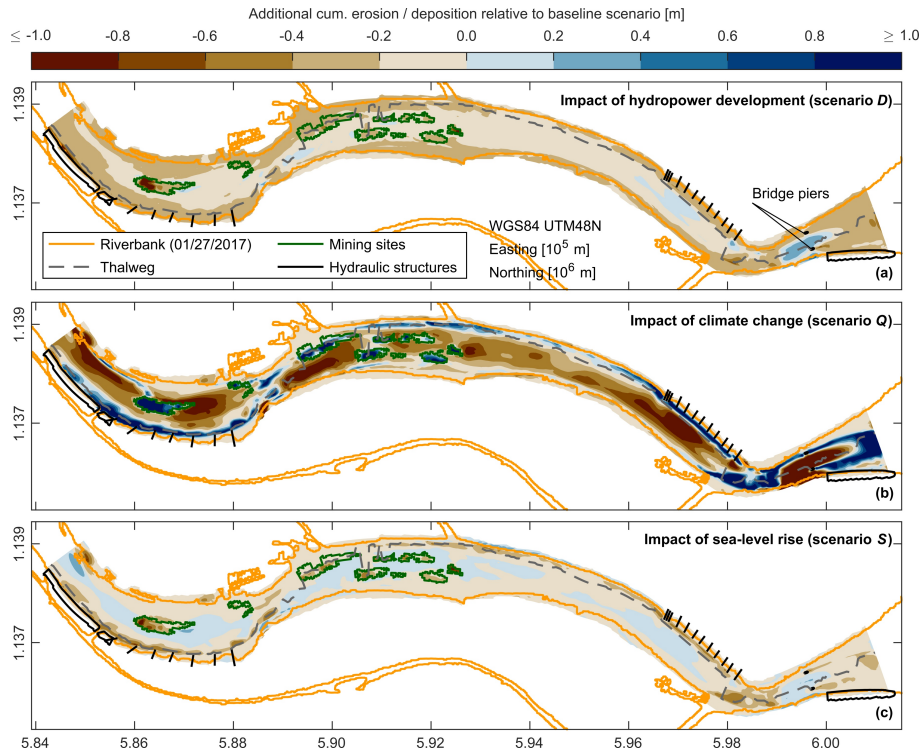


Figure 7. Patterns of additional cumulative erosion (red) and deposition (blue) in relation to the baseline scenario, including positions of riverbanks, the river’s thalweg, implemented sand mining sites and hydraulic structures. Riverbanks were extracted from historical Landsat-7 imagery using the MNDWI [38]. Landsat-7 images courtesy of the USGS, downloaded from the USGS EROS Centre (<https://earthexplorer.usgs.gov>). Sand mining sites were separated from the surrounding bathymetry using the approach in [6]. (a) Impact of hydropower development (scenario D) on the erosion and deposition pattern. (b) Impact of climate change-related increase in discharge (scenario Q) on the erosion and deposition pattern. (c) Impact of RSLR (scenario S) on the erosion and deposition pattern.

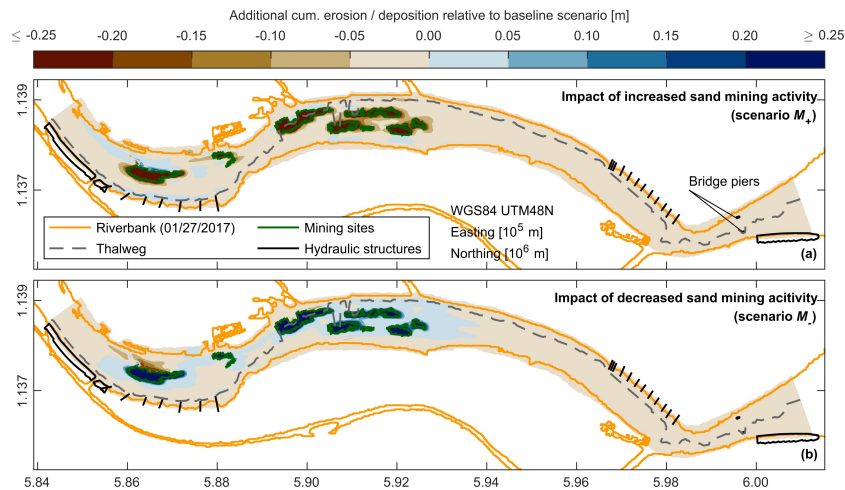


Figure 8. Patterns of additional cumulative erosion (red) and deposition (blue) in relation to the baseline scenario, including positions of riverbanks, the river’s thalweg, implemented sand mining sites and hydraulic structures. Riverbanks were extracted from historical Landsat-7 imagery using the MNDWI [38]. Landsat-7 images courtesy of the USGS, downloaded from the USGS EROS Centre (<https://earthexplorer.usgs.gov>). Sand mining sites were separated from the surrounding bathymetry using the approach in [6]. (a) Impact of increased sand mining activity (scenario M₊) on the erosion and deposition pattern. (b) Impact of decreased sand mining activity (scenario M₋) on the erosion and deposition pattern.

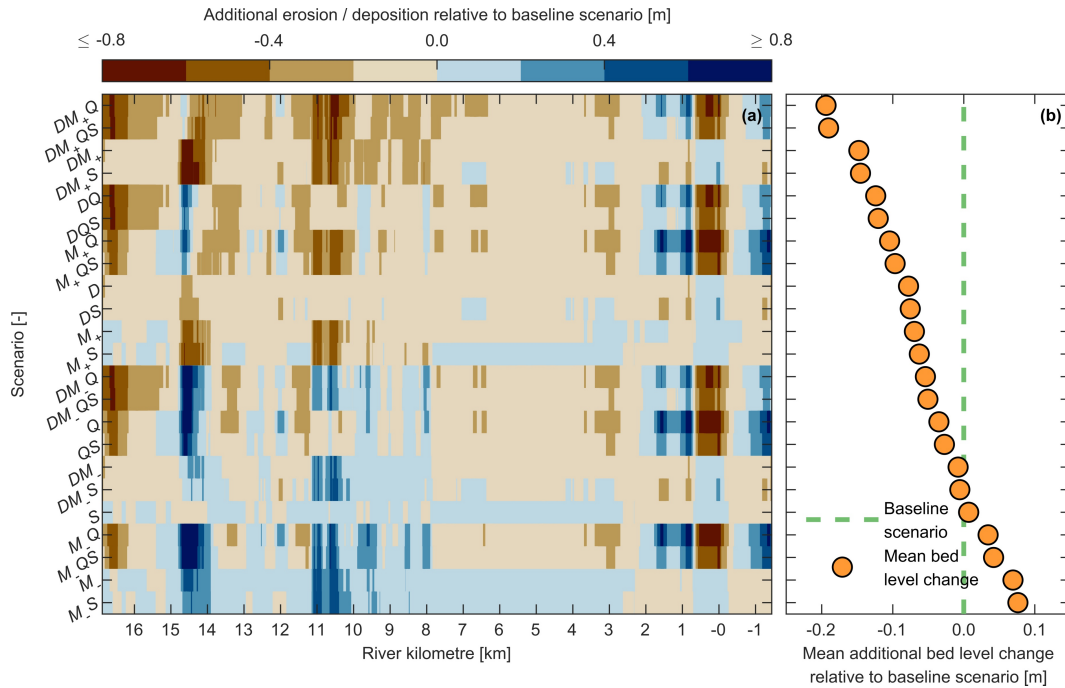


Figure 9. Mean bed level changes in relation to the baseline scenario. (a) Cross-sectional averages of bed level changes along the RKM system (see Figure 1a), indicating river sections of additional erosion (red) and deposition (blue) in relation to the baseline scenario. (b) Domain-wide averages of bed level changes in relation to the baseline scenario. Scenarios were sorted according to impact (from most additional deposition to most additional erosion). The notation of the scenarios is a combination of the individual driver notation listed in Table 2.

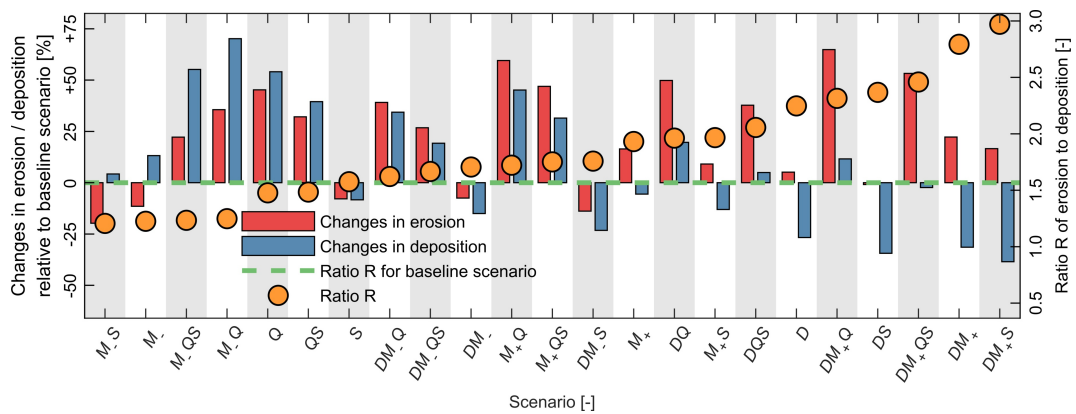


Figure 10. Domain-wide changes in total erosion and deposition volumes in relation to the baseline scenario as well as ratios between erosion and deposition volumes. Scenarios were sorted according to impact (from lowest to highest imbalance between erosion and deposition volumes). The notation of the scenarios is a combination of the individual driver notation listed in Table 2.

3.4. Impact of Climate Change (Scenario Q)

A climate change-induced increase in discharge leads to additional erosion for 49% of the study area, against 23% of additional deposition and approximately 25% of insignificant changes in relation to the baseline scenario (Figure 7b). Compared to other single drivers, this scenario shows the highest variability in bed level changes. The transport of sediment from shallower to deeper parts of the channel is amplified, likely leading to a gradual meandering of the river’s channel. Bed level changes are particularly prominent near RKM0 and 14, where deep scour holes have formed. Additionally, the refilling at sand mining locations is clearly accelerated for this scenario. On average, the bed level

incision is increased by approximately 31%, which equals a mean bed level change of -0.04 m (Figure 9). In relation to the baseline scenario, the imbalance between erosion and deposition volumes is even slightly reduced ($R_{\text{ero/dep},Q} = 1.48$) (Figure 10). A rise in the erosion volume by 45% is accompanied by an increase in deposition volume by 54%. Observed morphological changes relative to the baseline scenario are associated with an altered hydrodynamic forcing. The increased discharge induces higher flow velocities and bed shear stresses, thus mobilising and transporting more sediment from the riverbed. However, as indicated by the reduced imbalance of the local sediment budget, the amplified erosion is compensated by higher sediment supply from upstream (see Table 2) and a locally confined redistribution of sediments.

3.5. Impact of Sea Level Rise (Scenario S)

For the RSLR scenario, 19% of the study area exhibits additional erosion, against 33% of additional deposition and approximately 48% of insignificant changes (Figure 7c). Additional erosion mainly occurs near the riverbanks, while additional deposition mostly affects the central part of the river's channel. Sections of amplified channel deepening and sections of additional deposition are nearly in balance (Figure 9). In relation to the baseline scenario, the bed level even rises by 0.01 m on average, equivalent to a decrease in channel deepening by around -8% . The impact of RSLR on the ratio of erosion and deposition volumes within the study area is only minimal ($R_{\text{ero/dep},S} = 1.58$), as the erosion and deposition volumes are simultaneously reduced by -8% (Figure 10). Areas, which were barely elevated above the mean water level during the baseline scenario, are more frequently or even permanently inundated during the RSLR scenario. Those additional areas of shallow water likely favour the local settling of mud. Nevertheless, the overall transport of sediment is reduced in comparison to the baseline scenario (Table 2). Higher water levels due to RSLR decrease the local flow velocities and bed shear stresses in a similar manner as the hydropower impact scenario.

3.6. Cumulative Impacts of Multiple Drivers in Developed Scenarios

Across all scenarios, the incision patterns are very irregular. Compared to the baseline scenario, mean relative bed level changes vary between 0.08 and -0.19 m (Figure 9). The cumulative impact of multiple drivers can significantly exceed the impact of single drivers. The largest channel incision is associated with a combination of the impacts of hydropower development, a doubling of sand mining activity and a climate change-related increase in discharge (scenario DM_+Q). For this scenario, the channel deepening is increased by up to 146%. The total erosion volume across all scenarios varies between 5.78 and 11.87 $M m^3$, while the deposition volume varies between 2.83 and 7.82 $M m^3$. Even though some scenarios reduce the imbalance between erosion and deposition, none of the scenarios lead to a balanced environment, i.e., a ratio of $R_{\text{ero/dep}} \sim 1$. In relation to the baseline scenario, the imbalance between erosion and deposition volume is increased by up to 89% ($R_{\text{ero/dep},DM_+S} = 2.97$) in the case that the impacts of hydropower development, increased sand mining and RSLR are combined (scenario DM_+S) (Figure 10). This scenario is associated with an increase in erosion volume by 17%, accompanied by a decrease in deposition volume by -38% . It must be highlighted that the sum of changes in the erosion and deposition volumes for this scenario exceeds the cumulative volumetric changes of the involved single drivers. Caused by the interaction of multiple drivers, nonlinear processes likely amplify the impact on the local morphology. Furthermore, it becomes apparent that a complete prohibition of sand mining activity can counterbalance the impact of other drivers such as hydropower development (see scenarios D and DM_-), indicated by a significantly lower imbalance between the respective erosion and deposition volumes ($R_{\text{ero/dep},D} = 2.25$ and $R_{\text{ero/dep},DM_-} = 1.71$).

4. Discussion

In this study, the impacts of different scenarios with an inherent set and combination of drivers on the future morphological development of the VMD were quantified, exemplified by an 18 km stretch of the Tien River. Drivers included reductions in sediment supply and discharge

associated with hydropower development, sand mining activity, a climate change-related increase in discharge and RSLR. While existing numerical studies on the impacts of future scenarios on the VMD mainly concentrate on the river's future sediment dynamics [3,49], hydrology [11,27,59] and salinity intrusion [33,60,61], only recently has the response of the river's morphology gained attention within the scientific community [49]. Previous findings mainly concentrated on long-term erosion and deposition patterns within the estuaries and coastal zone of the VMD, neglecting impacts of climate change and RSLR, thus only focusing on three future scenarios [49]. In contrast, a high-resolution Delft3D model of the Tien River was used within this study to investigate a total of 23 possible future scenarios, including the impacts of climate change and RSLR. Besides erosion and deposition patterns, the results highlight tendencies for additional bed level incision and changes in the local erosion and deposition volumes. The findings in this study thus expand the existing knowledge in many aspects.

Based on boundary forcing for the baseline period, a mean bed level incision of approximately -0.13 m was observed. This simulation only focused on the wet season, as the local sediment transport is an order of magnitude higher during the wet season [6,35], compared to the dry season. Morphodynamic processes within the area are therefore mainly driven by the increased hydrodynamic forcing and sediment transport during the wet season. Accordingly, disregarding the dry season should only have a minimal impact on the overall results in general and on the actual rates of annual bed level incision in particular. This result is in good agreement with previous findings indicating a channel deepening of -0.13 to -0.50 m/yr [16,62]. Most investigated scenarios will increase the imbalance between the local erosion and deposition volumes, thus amplifying the trend of channel incision. Results show that hydropower development is the main driver for future erosional processes, followed by sand mining. This is in agreement with recent observations, which have linked rapid present-day bed level changes within the VMD mainly to the construction and operation of hydropower dams [16,62] and sand mining [5,6,16,17]. Furthermore, the results also indicate that drivers such as hydropower development can not only lead to significant morphological changes on the scale of decades [49], but also on a much smaller time scale (<1 year).

The possible consequences of these findings on the environment within the VMD are far-reaching. Bed level incision within the VMD was recently directly linked to salinity intrusion and an amplification of the tidal signal [16] as well as riverbank erosion [6,17]. Furthermore, river deepening is also known to trigger the import of mud into estuarine channels [63]. An increasing imbalance in the sediment budget of the Mekong River will also likely accelerate existing coastal erosion [23–25] and the loss of mangrove forests [26]. As the average thickness of alluvial sands is just approximately 28 m within the Lower Mekong [17], the delta region could run out of sand resources rather sooner than later, calling the delta's stability into question. A net loss of sediments will also affect the local ecology, groundwater levels and sediment composition [18–20]. Furthermore, indirect effects on the local agriculture and fishery sectors are likely [32,64].

Finally, one has to consider that the investigated scenarios almost exclusively represent the upper bound of plausible future developments within the VMD. Impacts thus could be lower if strategic planning limits the impact of hydropower infrastructure [65], necessary regulations are put into place to reduce the local sand mining activity [6,17] and global emissions are reduced [29]. Regarding the results of the sand mining scenarios, it must also be noted that only local sand mining activity is considered explicitly. A possible reduction in sediment supply to the study region as a consequence of upstream sand extraction was not included. Even though this effect of upstream sand mining is likely just minimal, it should only amplify rather than attenuate observed trends. Accordingly, the impact of sand mining on the local morphology could be higher than presented here.

5. Conclusions and Outlook

Based on in situ data, which was measured during the 2018 dry and wet seasons, a hydro-morphodynamic model was set up and validated, focusing on a stretch of the Tien River within the VMD. The model was nested into a well-calibrated hydrodynamic model of the whole

VMD [3,32], in order to generate boundary forcing for plausible future developments within the delta region. Mainly focusing on the upper bound of possible changes, the impacts of hydropower development, sand mining activity, climate change-related variations in discharge and RSLR on the local morphodynamics were analysed. The main findings are as follows.

- The study area must already be characterised as an erosional environment under present-day conditions, as indicated by the local imbalance between erosion and deposition and mean bed level changes.
- Based on tendencies for additional bed level incision and the local imbalance between erosion and deposition, hydropower development has the highest impact of all investigated drivers, followed by an increase in sand mining activity and a climate change-related increase in riverine discharge. A complete prohibition of local sand mining activity can counter the impact of other drivers on the local morphological processes, while the overall impact of RSLR is almost negligible.
- Nonlinear processes, which are caused by the interaction of multiple drivers, will likely lead to negative feedback effects on the evolution of the local bathymetry, thus amplifying prevailing erosional tendencies. The combination of hydropower development, increased sand mining and RSLR will lead to the largest imbalance in the local erosion and deposition budget ($R_{\text{ero/dep, DM+S}} = 2.97$). In relation to the baseline scenario, bed level incision can be amplified by up to 146%, caused by the cumulative effects of hydropower development, increased sand mining activity and a climate change-related increase in discharge.

The results highlight the need for a more sustainable future development of the VMD. Strategic hydropower planning on a basin-wide scale is needed to identify pathways that minimise the negative impacts of hydropower [65]. Furthermore, it is imperative to implement a management plan for local and basin-wide sand mining activity [6,17]. To prevent unsustainable or even informal practices, sand mining should be monitored closely. A complete prohibition of sand mining activity could mitigate the local net loss of sediments and therefore counter the impact of other drivers that amplify erosional processes.

Author Contributions: C.J., J.V., H.A. and T.S. designed the research framework. C.J., J.V., H.A. and T.S. planned the surveys. C.J. and N.V.D. designed the numerical experiments and performed the simulations. C.J. analysed the data and simulations. J.V. and T.S. contributed to many technical discussions. C.J. drafted the manuscript with input from J.V., N.V.D., H.A. and T.S. All authors have read and agreed to the published version of the manuscript.

Funding: Within the framework of the research project Catch-Mekong (<https://catchmekong.eoc.dlr.de>), this research was funded by the German Ministry of Education and Research (BMBF) under grant number 02WM1338D. The publication of this article was funded by the Open Access Fund of the Leibniz Universität Hannover.

Acknowledgments: We would like to thank all students who participated in the in situ measurements. Special thanks go to the team of the hydrological station of My Thuan (Vietnam) and the Center of Water Management and Climate Change (WACC) of Vietnam National University (VNU) for their support during the field surveys. Furthermore, we appreciate the provision of hydrological and topography data by the SRHMC and MONRE. Perceptually uniform colour-maps were used in this study to prevent visual distortion of the data [66,67].

Conflicts of Interest: The authors declare no conflict of interest.

Abbreviations

The following abbreviations are used in this manuscript.

ADCP	acoustic Doppler current profiler
BCC	bed composition generation
BSSp	adjusted Brier skill score
CTDs	multiparameter probes
DEM	digital elevation model
GCMs	general circulation models

LiDAR	light detection and ranging
MBES	multibeam echosounder
MNDWI	modified normalised difference water index
MONRE	Ministry of Natural Resources and Environment, Vietnam
MRB	Mekong River Basin
REV	relative error vector
RKM	river kilometre marker
RSLR	relative sea level rise
SRHMC	Southern Regional Hydro-Meteorological Center, Vietnam
SSCs	suspended sediment concentrations
USGS	United States Geological Survey
VMD	Vietnamese Mekong Delta

References

- Minderhoud, P.S.J.; Coumou, L.; Erkens, G.; Middelkoop, H.; Stouthamer, E. Mekong delta much lower than previously assumed in sea-level rise impact assessments. *Nat. Commun.* **2019**, *10*, 3847. [[CrossRef](#)]
- Kondolf, G.M.; Rubin, Z.K.; Minear, J.T. Dams on the Mekong: Cumulative sediment starvation. *Water Resour. Res.* **2014**, *50*, 5158–5169. [[CrossRef](#)]
- Manh, N.V.; Dung, N.V.; Hung, N.N.; Kумму, M.; Merz, B.; Apel, H. Future sediment dynamics in the Mekong Delta floodplains: Impacts of hydropower development, climate change and sea level rise. *Glob. Planet. Chang.* **2015**, *127*, 22–33. [[CrossRef](#)]
- Bravard, J.P.; Goichot, M.; Gaillot, S. Geography of Sand and Gravel Mining in the Lower Mekong River. *EchoGéo* **2013**, *26*. [[CrossRef](#)]
- Brunier, G.; Anthony, E.J.; Goichot, M.; Provansal, M.; Dussouillez, P. Recent morphological changes in the Mekong and Bassac river channels, Mekong delta: The marked impact of river-bed mining and implications for delta destabilisation. *Geomorphology* **2014**, *224*, 177–191. [[CrossRef](#)]
- Jordan, C.; Tiede, J.; Lojek, O.; Visscher, J.; Apel, H.; Nguyen, H.Q.; Quang, C.N.X.; Schlurmann, T. Sand mining in the Mekong Delta revisited - current scales of local sediment deficits. *Sci. Rep.* **2019**, *9*, 17823. [[CrossRef](#)] [[PubMed](#)]
- Syvitski, J.P.M.; Kettner, A.J.; Overeem, I.; Hutton, E.W.H.; Hannon, M.T.; Brakenridge, G.R.; Day, J.; Vörösmarty, C.; Saito, Y.; Giosan, L.; et al. Sinking deltas due to human activities. *Nat. Geosci.* **2009**, *2*, 681–686. [[CrossRef](#)]
- Tessler, Z.D.; Vörösmarty, C.J.; Overeem, I.; Syvitski, J.P.M. A model of water and sediment balance as determinants of relative sea level rise in contemporary and future deltas. *Geomorphology* **2018**, *305*, 209–220. [[CrossRef](#)]
- Kумму, M.; Lu, X.X.; Wang, J.J.; Varis, O. Basin-wide sediment trapping efficiency of emerging reservoirs along the Mekong. *Geomorphology* **2010**, *119*, 181–197. [[CrossRef](#)]
- Water, Land and Ecosystems in the Greater Mekong. Greater Mekong Dams Observatory.
- Dang, T.D.; Cochrane, T.A.; Arias, M.E.; Tri, V.P.D. Future hydrological alterations in the Mekong Delta under the impact of water resources development, land subsidence and sea level rise. *J. Hydrol. Reg. Stud.* **2018**, *15*, 119–133. [[CrossRef](#)]
- Xue, Z.; Liu, J.P.; Ge, Q. Changes in hydrology and sediment delivery of the Mekong River in the last 50 years: Connection to damming, monsoon, and ENSO. *Earth Surf. Process. Landforms* **2011**, *36*, 296–308. [[CrossRef](#)]
- Cochrane, T.A.; Arias, M.E.; Piman, T. Historical impact of water infrastructure on water levels of the Mekong River and the Tonle Sap system. *Hydrol. Earth Syst. Sci.* **2014**, *18*, 4529–4541. [[CrossRef](#)]
- Räsänen, T.A.; Someth, P.; Lauri, H.; Koponen, J.; Sarkkula, J.; Kумму, M. Observed river discharge changes due to hydropower operations in the Upper Mekong Basin. *J. Hydrol.* **2017**, *545*, 28–41. [[CrossRef](#)]
- Dugan, P.J.; Barlow, C.; Agostinho, A.A.; Baran, E.; Cada, G.F.; Chen, D.; Cowx, I.G.; Ferguson, J.W.; Jutagate, T.; Mallen-Cooper, M.; et al. Fish Migration, Dams, and Loss of Ecosystem Services in the Mekong Basin. *AMBIO* **2010**, *39*, 344–348. [[CrossRef](#)] [[PubMed](#)]
- Eslami, S.; Hoekstra, P.; Nguyen Trung, N.; Ahmed Kantoush, S.; Van Binh, D.; Duc Dung, D.; Tran Quang, T.; van der Vegt, M. Tidal amplification and salt intrusion in the Mekong Delta driven by anthropogenic sediment starvation. *Sci. Rep.* **2019**, *9*, 18746. [[CrossRef](#)]

17. Hackney, C.R.; Darby, S.E.; Parsons, D.R.; Leyland, J.; Best, J.L.; Aalto, R.; Nicholas, A.P.; Houseago, R.C. River bank instability from unsustainable sand mining in the lower Mekong River. *Nat. Sustain.* **2020**, *3*, 217–225. [[CrossRef](#)]
18. Kondolf, G.M. PROFILE: Hungry Water: Effects of Dams and Gravel Mining on River Channels. *Environ. Manag.* **1997**, *21*, 533–551. [[CrossRef](#)]
19. Peduzzi, P. Sand, rarer than one thinks. *Environ. Dev.* **2014**, *11*, 208–218. [[CrossRef](#)]
20. UNEP. *Sand and Sustainability: Finding New Solutions for Environmental Governance of Global Sand Resources*; GRID-Geneva, United Nations Environment Programme: Geneva, Switzerland, 2019.
21. Kumm, M.; Lu, X.X.; Rasphone, A.; Sarkkula, J.; Koponen, J. Riverbank changes along the Mekong River: Remote sensing detection in the Vientiane–Nong Khai area. *Quat. Int.* **2008**, *186*, 100–112. [[CrossRef](#)]
22. Miyazawa, N.; Sunada, K.; Sokhem, P. Bank erosion in the Mekong River basin: Is bank erosion in my town caused by the activities of my neighbors? In *Modern Myths of the Mekong*; Kumm, M., Keskinen, M., Varis, O., Eds.; Water & Development Publications, Helsinki University of Technology: Helsinki, Finland, 2008; pp. 19–26.
23. Anthony, E.J.; Brunier, G.; Besset, M.; Goichot, M.; Dussouillez, P.; Nguyen, V.L. Linking rapid erosion of the Mekong River delta to human activities. *Sci. Rep.* **2015**, *5*, 14745. [[CrossRef](#)]
24. Li, X.; Liu, J.P.; Saito, Y.; Nguyen, V.L. Recent evolution of the Mekong Delta and the impacts of dams. *Earth-Sci. Rev.* **2017**, *175*, 1–17. [[CrossRef](#)]
25. Luijendijk, A.; Hagenaars, G.; Ranasinghe, R.; Baart, F.; Donchyts, G.; Aarninkhof, S. The State of the World's Beaches. *Sci. Rep.* **2018**, *8*, 6641. [[CrossRef](#)] [[PubMed](#)]
26. Phan, L.K.; van Thiel de Vries, J.S.M.; Stive, M.J.F. Coastal Mangrove Squeeze in the Mekong Delta. *J. Coast. Res.* **2015**, *31*, 233–243. [[CrossRef](#)]
27. Lauri, H.; de Moel, H.; Ward, P.J.; Räsänen, T.A.; Keskinen, M.; Kumm, M. Future changes in Mekong River hydrology: Impact of climate change and reservoir operation on discharge. *Hydrol. Earth Syst. Sci.* **2012**, *16*, 4603–4619. [[CrossRef](#)]
28. Kingston, D.G.; Thompson, J.R.; Kite, G. Uncertainty in climate change projections of discharge for the Mekong River Basin. *Hydrol. Earth Syst. Sci.* **2011**, *15*, 1459–1471. [[CrossRef](#)]
29. Church, J.A.; Clark, P.U.; Cazenave, A.; Gregory, J.M.; Jevrejeva, S.; Levermann, A.; Merrifield, M.A.; Milne, G.A.; Nerem, R.S.; Nunn, P.D.; et al. Sea Level Change. In *Climate Change 2013: The Physical Science Basis. Contribution of Working Group I to the Fifth Assessment Report of the Intergovernmental Panel on Climate Change*; Stocker, T.F., Qin, D., Plattner, G.K., Tignor, M., Allen, S.K., Boschung, J., Nauels, A., Xia, Y., Bex, V., Midgley, P.M., Eds.; Cambridge University Press: Cambridge, UK; New York, NY, USA, 2013.
30. Erban, L.E.; Gorelick, S.M.; Zebker, H.A. Groundwater extraction, land subsidence, and sea-level rise in the Mekong Delta, Vietnam. *Environ. Res. Lett.* **2014**, *9*, 084010. [[CrossRef](#)]
31. Minderhoud, P.S.J.; Erkens, G.; Pham, V.H.; Bui, V.T.; Erban, L.; Kooi, H.; Stouthamer, E. Impacts of 25 years of groundwater extraction on subsidence in the Mekong delta, Vietnam. *Environ. Res. Lett.* **2017**, *12*, 064006. [[CrossRef](#)]
32. Manh, N.V.; Dung, N.V.; Hung, N.N.; Merz, B.; Apel, H. Large-scale suspended sediment transport and sediment deposition in the Mekong Delta. *Hydrol. Earth Syst. Sci.* **2014**, *18*, 3033–3053. [[CrossRef](#)]
33. Tran Anh, D.; Hoang, L.P.; Bui, M.D.; Rutschmann, P. Simulating Future Flows and Salinity Intrusion Using Combined One- and Two-Dimensional Hydrodynamic Modelling—The Case of Hau River, Vietnamese Mekong Delta. *Water* **2018**, *10*, 897. [[CrossRef](#)]
34. Lu, X.; Kumm, M.; Oeurng, C. Reappraisal of sediment dynamics in the Lower Mekong River, Cambodia. *Earth Surf. Process. Landforms* **2014**, *39*, 1855–1865. [[CrossRef](#)]
35. Thi Ha, D.; Ouillon, S.; Van Vinh, G. Water and Suspended Sediment Budgets in the Lower Mekong from High-Frequency Measurements (2009–2016). *Water* **2018**, *10*, 846. [[CrossRef](#)]
36. Stephens, J.D.; Allison, M.A.; Di Leonardo, D.R.; Weathers, H.D., III; Ogston, A.S.; McLachlan, R.L.; Xing, F.; Meselhe, E.A. Sand dynamics in the Mekong River channel and export to the coastal ocean. *Cont. Shelf Res.* **2017**, *147*, 38–50. [[CrossRef](#)]
37. Gugliotta, M.; Saito, Y.; Nguyen, V.L.; Ta, T.K.O.; Nakashima, R.; Tamura, T.; Uehara, K.; Katsuki, K.; Yamamoto, S. Process regime, salinity, morphological, and sedimentary trends along the fluvial to marine transition zone of the mixed-energy Mekong River delta, Vietnam. *Cont. Shelf Res.* **2017**, *147*, 7–26. [[CrossRef](#)]

38. Xu, H. Modification of normalised difference water index (NDWI) to enhance open water features in remotely sensed imagery. *Int. J. Remote Sens.* **2006**, *27*, 3025–3033. [[CrossRef](#)]
39. Lesser, G.R.; Roelvink, J.A.; van Kester, J.A.T.M.; Stelling, G.S. Development and validation of a three-dimensional morphological model. *Coast. Eng.* **2004**, *51*, 883–915. [[CrossRef](#)]
40. Deltares. *Delft3D-FLOW—User Manual, Simulation of Multi-Dimensional Hydrodynamic Flows and Transport Phenomena, Including Sediments*; Deltares: Delft, The Netherlands, 2020.
41. van Rijn, L.C. Unified View of Sediment Transport by Currents and Waves. I: Initiation of Motion, Bed Roughness, and Bed-Load Transport. *J. Hydraul. Eng.* **2007**, *133*, 649–667. [[CrossRef](#)]
42. Wolanski, E.; Ngoc Huan, N.; Trong Dao, L.; Huu Nhan, N.; Ngoc Thuy, N. Fine-sediment Dynamics in the Mekong River Estuary, Vietnam. *Estuar. Coast. Shelf Sci.* **1996**, *43*, 565–582. [[CrossRef](#)]
43. Wolanski, E.; Huu Nhan, N.; Spagnol, S. Sediment Dynamics During Low Flow Conditions in the Mekong River Estuary, Vietnam. *J. Coast. Res.* **1998**, *14*, 472–482.
44. Partheniades, E. Erosion and Deposition of Cohesive Soils. *J. Hydraul. Div.* **1965**, *91*, 105–139.
45. Krone, R.B. *Flume Studies of the Transport of Sediment in Estuarial Shoaling Processes; Final Report*; Hydraulic Engineering Laboratory and Sanitary Engineering Research Laboratory, University of California: Berkeley, CA, USA, 1962.
46. Winterwerp, J.C.; van Kesteren, W.G.M. *Introduction to the Physics of Cohesive Sediment Dynamics in the Marine Environment*, 1st ed.; Elsevier B.V.: Amsterdam, The Netherlands, 2004.
47. Duy Vinh, V.; Ouillon, S.; Van Thao, N.; Ngoc Tien, N. Numerical Simulations of Suspended Sediment Dynamics Due to Seasonal Forcing in the Mekong Coastal Area. *Water* **2016**, *8*, 255. [[CrossRef](#)]
48. Thanh, V.Q.; Reyns, J.; Wackerman, C.; Eidam, E.F.; Roelvink, D. Modelling suspended sediment dynamics on the subaqueous delta of the Mekong River. *Cont. Shelf Res.* **2017**, *147*, 213–230. [[CrossRef](#)]
49. Tu, L.X.; Thanh, V.Q.; Reyns, J.; Van, S.P.; Anh, D.T.; Dang, T.D.; Roelvink, D. Sediment transport and morphodynamical modeling on the estuaries and coastal zone of the Vietnamese Mekong Delta. *Cont. Shelf Res.* **2019**, *186*, 64–76. [[CrossRef](#)]
50. Gratiot, N.; Bildstein, A.; Anh, T.T.; Thoss, H.; Denis, H.; Michallet, H.; Apel, H. Sediment flocculation in the Mekong River estuary, Vietnam, an important driver of geomorphological changes. *Comptes Rendus Geosci.* **2017**, *349*, 260–268. [[CrossRef](#)]
51. Brownlie, W.R. Flow Depth in Sand-Bed Channels. *J. Hydraul. Eng.* **1983**, *109*, 959–990. [[CrossRef](#)]
52. van der Wegen, M.; Dastgheib, A.; Jaffe, B.E.; Roelvink, D. Bed composition generation for morphodynamic modeling: Case study of San Pablo Bay in California, USA. *Ocean Dyn.* **2011**, *61*, 173–186. [[CrossRef](#)]
53. Roelvink, J.A. Coastal morphodynamic evolution techniques. *Coast. Eng.* **2006**, *53*, 277–287. [[CrossRef](#)]
54. Ranasinghe, R.; Swinkels, C.; Luijendijk, A.; Roelvink, D.; Bosboom, J.; Stive, M.; Walstra, D. Morphodynamic upscaling with the MORFAC approach: Dependencies and sensitivities. *Coast. Eng.* **2011**, *58*, 806–811. [[CrossRef](#)]
55. Blom, A. Different approaches to handling vertical and streamwise sorting in modeling river morphodynamics. *Water Resour. Res.* **2008**, *44*, W03415. [[CrossRef](#)]
56. Ta, T.K.O.; Nguyen, V.L.; Tateishi, M.; Kobayashi, I.; Tanabe, S.; Saito, Y. Holocene delta evolution and sediment discharge of the Mekong River, southern Vietnam. *Quat. Sci. Rev.* **2002**, *21*, 1807–1819. [[CrossRef](#)]
57. van Rijn, L.C.; Walstra, D.J.R.; Grasmeijer, B.; Sutherland, J.; Pan, S.; Sierra, J.P. Simulation of nearshore hydrodynamics and morphodynamics on the time scale of storms and seasons using process-based profile models. In *Coast3D—Egmond: The Behaviour of a Straight Sandy Coast on the Time Scale of Storms and Seasons: Process Knowledge and Guidelines for Coastal Management: End Document, March 2002*; van Rijn, L.C., Ruessink, B.G., Mulder, J.P.M., Eds.; Aqua Publications: Amsterdam, The Netherlands, 2002; pp. S1–S33.
58. Sutherland, J.; Peet, A.H.; Soulsby, R.L. Evaluating the performance of morphological models. *Coast. Eng.* **2004**, *51*, 917–939. [[CrossRef](#)]
59. Van, P.D.T.; Popescu, I.; van Griensven, A.; Solomatine, D.P.; Trung, N.H.; Green, A. A study of the climate change impacts on fluvial flood propagation in the Vietnamese Mekong Delta. *Hydrol. Earth Syst. Sci.* **2012**, *16*, 4637–4649. [[CrossRef](#)]
60. Khang, N.D.; Kotera, A.; Sakamoto, T.; Yokozawa, M. Sensitivity of Salinity Intrusion to Sea Level Rise and River Flow Change in Vietnamese Mekong Delta-Impacts on Availability of Irrigation Water for Rice Cropping. *J. Agric. Meteorol.* **2008**, *64*, 167–176. [[CrossRef](#)]

61. Smajgl, A.; Toan, T.Q.; Nhan, D.K.; Ward, J.; Trung, N.H.; Tri, L.Q.; Tri, V.P.D.; Vu, P.T. Responding to rising sea levels in the Mekong Delta. *Nat. Clim. Chang.* **2015**, *5*, 167–174. [[CrossRef](#)]
62. Binh, D.V.; Kantoush, S.; Sumi, T. Changes to long-term discharge and sediment loads in the Vietnamese Mekong Delta caused by upstream dams. *Geomorphology* **2020**, *353*, 107011. [[CrossRef](#)]
63. Dyer, K.R. *Estuaries: A Physical Introduction*, 2nd ed.; John Wiley & Sons: Chichester, UK, 1997.
64. Valbo-Jørgensen, J.; Coates, D.; Hortle, K. Fish Diversity in the Mekong River Basin. In *The Mekong*; Campbell, I.C., Ed.; Academic Press: Sand Diego, CA, USA, 2009; pp. 161–196. [[CrossRef](#)]
65. Schmitt, R.J.P.; Bizzi, S.; Castelletti, A.; Opperman, J.J.; Kondolf, G.M. Planning dam portfolios for low sediment trapping shows limits for sustainable hydropower in the Mekong. *Sci. Adv.* **2019**, *5*, eaaw2175. [[CrossRef](#)] [[PubMed](#)]
66. Cramer, F. Scientific colour-maps. *Zenodo* **2018**, [[CrossRef](#)]
67. Cramer, F. Geodynamic diagnostics, scientific visualisation and StagLab 3.0. *Geosci. Model Dev.* **2018**, *11*, 2541–2562. [[CrossRef](#)]

Sample Availability: Measured datasets and model input files can be acquired from the corresponding author upon reasonable request.



© 2020 by the authors. Licensee MDPI, Basel, Switzerland. This article is an open access article distributed under the terms and conditions of the Creative Commons Attribution (CC BY) license (<http://creativecommons.org/licenses/by/4.0/>).